RSC Advances

PAPER

Cite this: *RSC Adv.*, 2024, **14**, 25062

Microstructure tuned $Na_3V_2(PO_4)_3$@C electrodes toward ultra-long-life sodium-ion batteries†

Ranjit S. Kate,[ab] Kaustav Bhattacharjee,[b] Milind V. Kulkarni,[b] Bharat B. Kale,*[bc] Ramesh J. Deokate *[a] and Ramchandra S. Kalubarme *[b]

Received 9th June 2024
Accepted 23rd July 2024

DOI: 10.1039/d4ra04221b

rsc.li/rsc-advances

Sodium-ion batteries (SIBs) are emerging as the best replacement for Li-ion batteries. In this regard, research on developing a reliable cathode material for SIBs is burgeoning. Rhombohedral $Na_3V_2(PO_4)_3$ (NVP), is a typical sodium super ionic conductor (NASICON) type material having prominent usage as a cathode material for SIBs. In this study, we prepared an NVP@C composite using a one-step hydrothermal method (at 180 °C) and consecutively calcined at different temperatures (750, 800, 850, and 900 °C). All the samples were thoroughly characterized and the changes in the crystal structure and particle size distribution were investigated using a Rietveld refinement method. NVP calcined at 850 °C exhibits the best battery performance with a discharge capacity of 94 mA h g^{-1} and retention up to 90% after 250 cycles at 2C. It also exhibits remarkable cycling stability with 94% (63 mA h g^{-1}) retention after 2000 cycles at high-rate endurance (10C). The observed electrochemical performances of the samples were correlated with improved electrical conductivity due to the conductive carbon mixing with $Na_3V_2(PO_4)_3$ and enhancement in the crystallinity.

1. Introduction

The rapid development of human society, excessive reliance on fossil fuels, and global concerns over climate change have led to the emergence of green and sustainable energy alternatives *i.e.* solar, wind, tidal, and geothermal sources to meet the world's rising energy needs.[1,2] However, the energy produced from these sources is intermittent and dependent on the environmental conditions. To combine these intermittent energy supplies into the grid effectively, the requirement for an efficient energy storage system is inevitable. Among the different types of energy storage technologies, batteries are promising alternatives. SIBs are considered a highly promising high-performance energy storage devices compared to their lithium-ion counterpart, due to abundant sodium resources, lower price, suitable redox potential, and similar intercalation chemistry with lithium-ion batteries (LIBs).[3–6] However, Na^+ has a greater ionic radius (0.102 nm) compared to that of Li^+ (0.076 nm), and SIBs usually exhibit weak rate capability, and limited cycle longevity.[7,8] Additionally, the greater Na^+ induces volume expansion/contraction triggering the structural distortion in the electrode materials.[9,10] Therefore, a host material with adequate interstitial spaces and open crystallographic structure is strongly recommended for rapid sodium ion storage.

In this context, a variety of positive electrode materials such as transition metal oxides,[11–13] polyanion compounds,[14,15] ferrocyanide materials,[16,17] organic compounds,[18] and Prussian blue-type[19,20] materials have been extensively investigated. Among these cathode materials for SIBs, polyanionic compounds have been most favoured due to better safety, longer cycle life, and high operating potential.[21,22] Polyanion-type NVP with a typical 3D NASICON structure has gained attention as a cathode material because of its high energy density (~400 W h kg^{-1}), impressive theoretical capacity (117 mA h g^{-1}), good thermal stability, and moderate potential plateau of ~3.4 V (*vs.* Na/Na^+).[23–25] Additionally, it can be used as an anode that delivers a capacity of 75 mA h g^{-1} at 1.6 V *vs.* Na/Na^+.[26] Therefore, it is possible to fabricate a symmetric SIB with outstanding safety by utilizing the NVP as a cathode and anode. However, the electrical conductivity of NVP is low and it is a prime hurdle, impacting its useable capacity. To mitigate this drawback two promising methodologies have been used so far: (i) reduce the particle size of the NVP to the nanoscale to shorten the electron's path length,[27] and (ii) coating the conductive layer to provide a conductive framework and accommodate the volume change associated with the insertion/de-insertion of Na-ions.[28,29] Along with the inherent properties of electrode material, crystallinity, electrochemical activity, and many other characteristics of the synthesized materials are

[a]*Vidya Pratishthan's Arts, Science and Commerce College, Vidyanagari, Baramati 413133, India. E-mail: deokate2000@yahoo.co.in*

[b]*Centre for Materials for Electronics Technology, Panchavati, Off. Dr Homi Bhabha Road, Pashan, Pune 411008, India. E-mail: kchandra_82@yahoo.co.in; bbkale1@gmail.com*

[c]*MIT World Peace University (MIT-WPU), Paud Rd, Kothrud, Pune, Maharashtra 411038, India. E-mail: bbkale1@gmail.com*

† Electronic supplementary information (ESI) available. See DOI: https://doi.org/10.1039/d4ra04221b

influenced by the calcination temperature. However, the hydrothermal approach has not yet been used to evaluate the impact of calcination temperature on the physico-chemical and electrochemical properties of NVP@C.

In the present work, the electrical conductivity of NVP was improved by employing the hydrothermal synthesis method by *in situ* carbon coating (NVP@C). This study is the first to explore the impact of different calcination temperatures on the electrochemical properties of NVP@C, using detailed characterization with a focus on phase purity through Rietveld refinement analysis. Our work provides comprehensive insights into how calcination conditions affect battery performance, including capacity retention, rate capability, and cycle life. The optimum NVP@C exhibits the high initial discharge capacities of 103 and 67 mA h g^{-1} at 0.1C and 10C rates with better rate-capability and cyclability, suggesting a prospective application as a positive electrode material for SIBs.

2. Experimental

2.1. Synthesis of $Na_3V_2(PO_4)_3$@C

In a typical synthesis, based on the method described by Duan *et al.*,[30] 6 mmol Na_2CO_3, 4 mmol V_2O_5, and 12 mmol $NH_4H_2PO_4$ were dissolved in 70 mL of distilled water and stirred at room temperature. Then, 6 mmol of ascorbic acid was introduced, resulting in the formation of a blue suspension, which underwent stirring for 30 minutes before being transferred into a 100 mL Teflon-lined autoclave. The autoclave was sealed and kept at 180 °C for 40 hours, then allowed to naturally cool to room temperature. Subsequently, the resulting brown mixture underwent ultrasonic treatment for 60 minutes to attain uniform dispersion, followed by heating at 80 °C with stirring to evaporate water, and finally drying overnight at 120 °C. This resultant complex underwent thorough grinding and preheated at 350 °C for 4 hours in an Ar + H_2 (95 : 5) atmosphere. The preheated sample was then crushed into a powder and calcined for 6 h in the same atmosphere at different temperatures such as 750, 800, 850, and 900 °C. The synthesized samples were denoted as NH1, NH2, NH3, and NH4, respectively. Scheme 1 outlined the experimental procedure for synthesizing the NVP@C cathode material.

2.2. Material characterization

For the characterization of crystallographic phases and for analyzing the microstructure and crystal structure parameters of all the synthesized NVP@C samples, powder X-ray diffraction (PXRD) analyses were conducted using a Bruker Advanced D8 instrument with Cu-Kα (λ = 0.1548 Å) radiation source. The measurements employed Bragg–Brentano goniometer geometry, with a step size of 0.02° and stepping time of 4 s, covering the 2θ range from 10 to 80°. For the Rietveld refinement analyses, the PXRD data were analyzed using the MAUD. Raman spectra were obtained using a Renishaw Invia Raman microscope featuring a 532 nm laser. The carbon content was quantified employing a VarioEL III elemental analyzer (Elementar, Germany). Four-point DC measurements were performed to quantify the electronic conductivity of the calcined samples. The microstructure of the samples was observed using Field emission scanning electron microscopy (FESEM, Hitachi, S-4800) and field emission transmission electron microscopy (FETEM by JEOL; JEM-2200FS). X-ray photoelectron spectroscopy (XPS) analysis was performed with the Thermo Fisher Scientific Co., Theta Probe. The surface area and porosity of the samples were assessed using Brunauer–Emmett–Teller analysis (BET: Quantachrome TouchWin v1.11).

2.3. Electrochemical characterization

The electrochemical tests of NVP@C samples were performed by fabricating CR2032-type coin cells with electrodes having a diameter of 16 mm. The cathode slurry comprised 80% of the active material, 10% conducting carbon, and 10% PVDF in *N*-methyl-2-pyrrolidone. After thorough mixing, the slurry was evenly coated onto an aluminium foil with a thickness of 60 microns and dried at 120 °C for 12 hours in a vacuum oven. The typical loading mass of active material is around 3 mg for every electrode. For the counter electrode, sodium metal foil was used, and 1 M $NaClO_4$ in a 1 : 1 volume ratio of ethylene carbonate (EC) and diethyl carbonate (DEC) served as the electrolyte, with an amount of 120 microliters. Whatman Glass Microfiber Filter was employed as the separator material. All the coin cells were fabricated in an argon-filled glove box. The cyclic voltammetry of the half NVP@C cells was examined using a potentiostat/galvanostatic instrument (Metrohm Autolab) in the potential range of 2.8–4 V with a scan rate of 0.1 mV s^{-1}. Galvanostatic charge/discharge (GCD) tests were executed at various C-rates within the 2.8–4.0 V range. Electrochemical impedance spectroscopy (EIS) measurements of freshly fabricated and cycled cells were performed at an amplitude of 5 mV with the applied frequency ranging from 0.1 Hz to 1 MHz. All the electrochemical measurements were performed at 298 K.

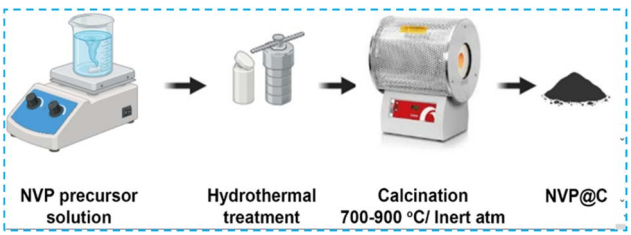

Scheme 1 Synthesis process of the $Na_3V_2(PO_4)_3$@C samples.

3. Results & discussion

Fig. S1(a)† shows the PXRD patterns of various NVP@C samples. All diffraction peaks match the rhombohedral NVP phase (space group: *R3c*, JCPDS card no. 00-062-0345). Unlike others, the NH1 sample shows unusual background intensities within the 2θ range of 25–35°. The reason is the inadequate crystallinity of the NVP material at 750 °C and the presence of amorphous carbon impurities contributing to the total intensity. While the other calcined samples show sharp diffraction

peaks corresponding to crystalline NVP phase. Fig. S1(b)† shows the Raman spectra of different NVP@C samples within the frequency range 500–2000 cm^{-1}. The spectra contain two characteristic peaks that correspond to the D-band and G-band of carbon material.[31] It is believed that subjecting calcination at elevated temperatures causes the development of a carbon layer on the surface of the NVP particles. Sample NH2 and NH3 show slightly higher I_D/I_G ratios, indicating more defects or incomplete graphitization compared to NH1 and NH4. These differences underscore subtle variations in structural properties due to different calcination conditions.

To support this observation, we used a carbon–sulfur analyzer to quantify the carbon content in the materials which resulted in 7.60, 7.44, 4.33, and 4.03% of carbon for the NH1, NH2, NH3, and NH4 samples, respectively. In Raman measurements, the carbon on the particle surface predominantly absorbs the incoming laser radiation, hindering the light from reaching the core material and thereby diminishing the signal of NVP in the corresponding spectra. The background-subtracted Raman spectra were then used to calculate the I_D/I_G ratio which falls in the range 0.85–0.89 for all the samples. This indicates that the NVP@C samples contain a significant amount of sp^2-hybridized carbon moieties, which ultimately enhance the electronic conductivity at the particle interfaces.

Electronic conductivity was measured using the four-point measurement setup. The electronic conductivity was found to be 4.051224×10^{-3} S cm^{-1}, 6.338602×10^{-3} S cm^{-1}, 1.625008×10^{-2} S cm^{-1}, and 7.519707×10^{-3} S cm^{-1} for the calcination temperature 750, 800, 850 and 900 °C, respectively. The higher conductivity at 850 °C is likely due to optimal phase formation, improved carbon coating uniformity, and enhanced microstructure resulting in better electron flow. Additionally, higher phase purity at this temperature further contributes to the increased conductivity.

Fig. 1(a) depicts the Rietveld analysis of the PXRD patterns for all the NVP samples. The experimental data were fitted with the help of MAUD software[32] using the standard crystallographic information file for NVP as reported by Zatovsky.[33] The pseudo-Voigt (pV) peak shape function with asymmetry and a background polynomial function of degree 4 was considered. Sequential refinements of the (1) background and scale parameters, (2) basic phase parameter, (3) microstructure (size and strain), and (4) crystal structure (lattice parameters, partial occupancy factor, fractional coordinate, and spherical harmonics) parameters were performed for each the refinement analysis according to the following equation, sample. A log-normal distribution model was implemented in[34]

$$f(R) = R^{-1}[2\pi \ln(1+c)]^{-1/2}\exp\left\{\frac{\ln^2\left[R\bar{R}^{-1}(1+c)^{1/2}\right]}{[2\ln(1+c)]}\right\}$$

where $\bar{R}$ is the lognormal mean size, and the dimensionless ratio c is defined by $\frac{\sigma_R{}^2}{\bar{R}^2}$, where $\sigma_R{}^2$ denotes dispersion of the distribution. According to the literature, the line profile represented by the second derivative of the Fourier cosine coefficient is proportional to the unit cell column length in the direction of the diffraction vector. The volume weighted ($\langle D_V \rangle$) and area weighted ($\langle D_A \rangle$) domain sizes were calculated from the following equations,

$$\langle D_V \rangle = \frac{3\bar{R}(1+c)^3}{2} \text{ and } \langle D_A \rangle = \frac{4\bar{R}(1+c)^2}{3}.$$

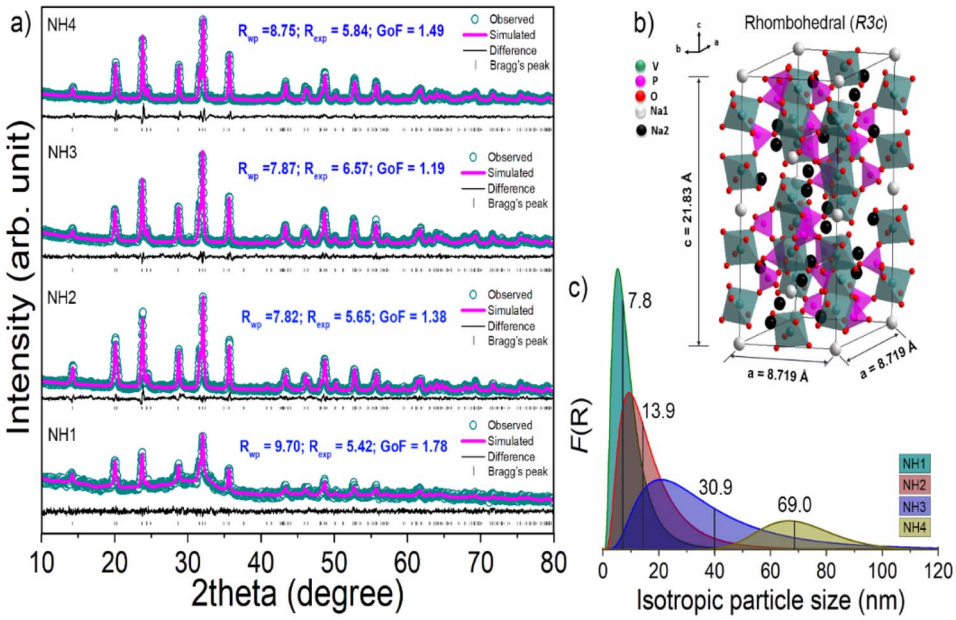

Fig. 1 (a) PXRD fitting analyses of the NVP@C samples by Rietveld refinement method. Different fitting reliability indices are shown in the inset. (b) Representation of typical rhombohedral (space group *R3c*) NVP crystal lattice (view along the (010) direction) after the refinement analysis of the NH_3 sample. (c) Lognormal distributions of particle size along with corresponding lognormal mean sizes for different NVP@C samples obtained *via* Rietveld refinement analyses.

Table 1 Rietveld refined parameters for different NVP@C samples

Rhombohedral $Na_3V_2(PO_4)_3$; space group: *R3c*				
Calcination temperature (°C)	750	800	850	900
Refined parameters				
Lattice parameters				
a (Å)	8.7270	8.7198	8.7190	8.7204
c (Å)	21.78	21.80	21.83	21.80
c/a	2.4957	2.5006	2.5040	2.4999
Volume (Å^3)	1481.48	1481.96	1483.66	1481.72
Lognormal mean size ($\bar{R}$/nm)	7.8	13.9	30.9	69.0
Variance ($\sigma_R{}^2$/nm)	0.625	0.63	0.633	0.2
$c = \sigma R^2/\bar{R}^2$	0.01	0.003	6.6×10^{-4}	4.2×10^{-5}
$\langle D_V \rangle$/nm	12.05	21.03	46.44	103.51
$\langle D_A \rangle$/nm	10.61	18.64	41.25	138.01

The quality of the fitting was assessed by checking the goodness of fit (GoF) value which is typically 1, and two reliability parameters R_{exp} and R_{wp}, which must be close to or less than 10%.[35] Table S1† shows the list of different lattice parameters for the NH3 sample obtained from the refinement analyses. From Table 1 it is clear that with an increase in calcination temperature, the $\langle D_V \rangle$ and $\langle D_A \rangle$ values increase linearly. The results also indicate that the unit cell volumes of NVP samples increase with calcination temperature which is favorable for the insertion and de-insertion of sodium ions. The typical rhombohedral unit cell representation as shown in Fig. 1(b) was obtained after importing the refined crystallographic information file of the NH3 sample into the 'Diamond' software. Such depiction aids in understanding the 3D open framework structure of the compound, which is created by the interconnection of VO_6 octahedra and PO_4 tetrahedra, ultimately forming a $[V_2(PO_4)_3]$ framework through corner-sharing. Two types of Na^+ ions (Na1 and Na2) are also identified within the crystal lattice with two distinct sites such as Na1 and Na2. A representative molecular fragment of the unit cell is shown in Fig. S2 (ESI†) to understand the Na^+ ions coordination environments. Different Na–O bond lengths are calculated and shown in Fig. S2.† Fig. 1(c) shows the isotropic particle size distribution of the NH1, NH2, NH3, and NH4 samples. The distributions were obtained through the Rietveld refinement analysis, revealing particle sizes with peaks at 7.8 nm, 13.9 nm, 30.9 nm, and 69.0 nm for NH1, NH2, NH3, and NH4, respectively. The distributions indicate a broad range of particle sizes.

The morphology of the synthesized NVP@C samples was examined by FESEM. Fig. S3† shows the morphologies of the NVP@C samples calcined at various temperatures. Each sample appeared as an agglomerated particulate type with typical surface coating characteristics. The presence of carbon in all the samples is already been proved by Raman spectroscopy. Nevertheless, the particles become less tightly bound when subjected to higher temperatures during calcination. After increasing the calcination temperature to 900 °C, the particles have grown and formed large heterogeneous particles.

Fig. 2(a) and (b) presents FETEM images of the NH3 sample. As evident, the NVP particles are agglomerated and covered with carbon layers. Moreover, the particles are connected through carbon residue which is advantageous for enhanced electronic conductivity. Fig. 2(c) shows the HRTEM image illustrating the coating of carbon layer around the NVP particles. HRTEM image and the corresponding inverse fast Fourier transformed (FFT) image of a selected area of the sample are shown in Fig. 2(d), respectively. The HRTEM image (Fig. 2(d)) shows clear lattice fringes with a d-spacing of 0.41 nm, which corresponds to the interplanar distance of the (104) plane of rhombohedral NVP crystal. The EDS elemental mapping of the NH3 sample is performed to understand the distribution of the elements. A grayscale image of the sample is shown in Fig. 2(e) and the corresponding elemental mapping was indicated side-by-side at the bottom row of Fig. 2.

Further, XPS measurements were conducted to understand the chemical composition and oxidation states of synthesized NVP@C. Fig. S4(a)† shows the survey spectrum which reveals the presence of V, P, O, C, and Na elements in NVP. Fig. S4(b)† illustrates the deconvolution of the V 2p peaks into two peaks located at 516.9 and 523.9 eV, indicating the presence of V^{3+}.[36] Peak with a binding energy of 133.8 eV (Fig. S4c†) corresponding to the 2p state of P. XPS spectra of C 1s in Fig. S4(d)† shows three bonding configurations located at 284.1 eV (C–C), 285.8 eV (C–O) and 288.1 eV (C=O), respectively.[37,38] In Fig. S4(e),† the high-resolution Na 1s spectrum displays a peak at 1071.7 eV, indicating the presence of Na.

Fig. S5† shows the nitrogen adsorption–desorption isotherms of NVP@C samples calcined at different temperatures. Hysteresis loops between the adsorption and desorption curves show type III isotherm indicating weak interaction between solid and gas. The specific surface area of NVP@C samples is found to be 9, 13, and 17 $m^2\ g^{-1}$ for samples NH2, NH3, and NH4, respectively. An increase in surface area was observed owing to the particle separation with an increase in calcination temperature. The inset in Fig. S5† illustrates the pore size distribution of the NVP@C after calcination at various temperatures, highlighting the presence and distribution of both mesopores and macropores. The BET surface area, pore volume, and pore diameter of the samples calcined at various temperatures are summarized in Table S2 (ESI†).

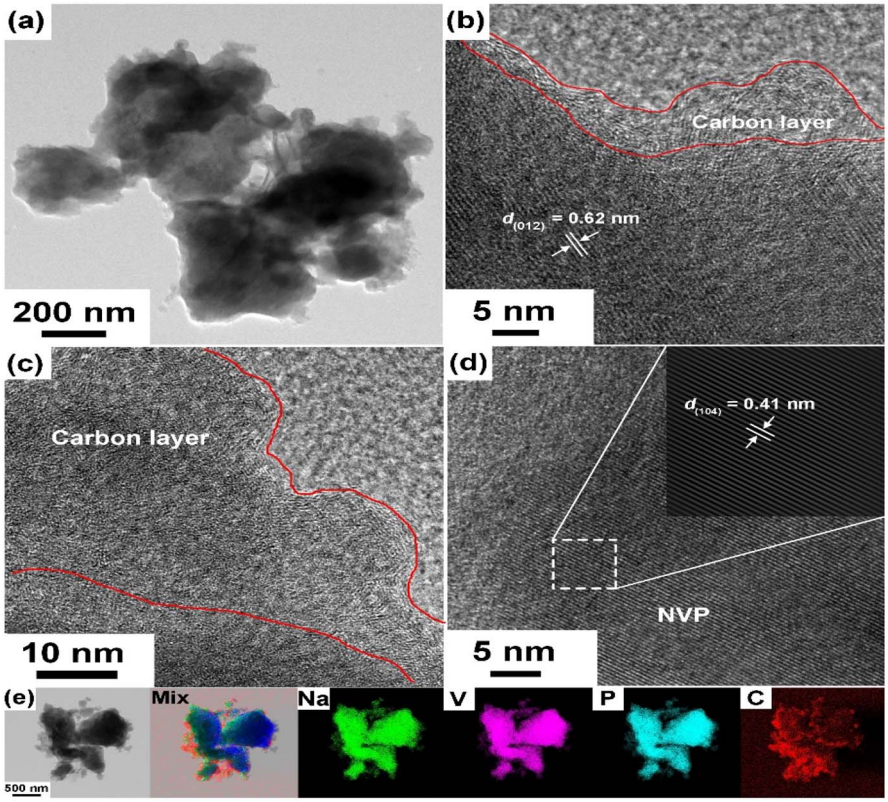

Fig. 2 FETEM images of NVP@C calcined at 850 °C (a) and (b) FETEM images at low and high magnifications, (c) HRTEM image highlighting the carbon layer, (d) FFT corresponding to the HRTEM, (e) EDX mapping, and corresponding elemental distributions of Na, V, P, C.

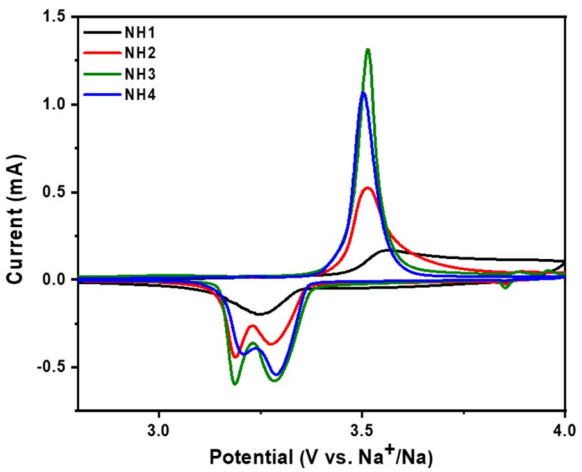

Fig. 3 1st Cyclic voltammetry (CV) curves of the NVP@C cycled between 2.8 and 4.0 V at a scan rate of 0.1 mV s^{-1} calcined at different temperatures.

Fig. 3 illustrates the initial CV scan of NVP@C for different temperatures within the potential range of 2.8–4.0 V at a scan rate of 0.1 mV s^{-1}. As depicted in the figure, the nature of the curves for all four electrodes is similar, displaying clear oxidation and reduction peaks. Sharp oxidation peaks are observed at about 3.51 V for all electrodes which are attributed to the extraction of Na^+ from NVP@C. However, the single reduction peak obtained for NH1 (750 °C) corresponds to the intercalation of sodium ions into the crystal structure. Further, for other samples, two reduction peaks were observed at 3.28 and 3.19 V during the insertion of sodium-ion. The split in reduction peak is attributed to the rearrangement of the local redox environment resulting from the migration of Na ions from Na(1) to the Na(2) sites.[39]

Fig. 3 illustrates that the peak current significantly rises with a rise in calcination temperature, exhibiting reduced polarization (Table S3†), suggesting an enhancement in sodium ion transport and reaction kinetics due to calcination treatment. Fig. S6 (ESI†) exhibits the CV curves of NVP@C samples for the initial cycles, conducted between 2.5 and 4.0 V (*vs.* Na^+/Na) at a scan rate of 0.1 mV s^{-1}. Table S3† indicates that except NVP@C calcined at 750 °C, all samples demonstrate the minimum potential difference. This suggests that the polarization degree of the material is small, leading to enhanced reversibility of Na^+ de-intercalation and intercalation.

The charge–discharge curves at 0.1–5C rates for the samples synthesized at different temperatures are shown in Fig. S7 (ESI†). All the NVP@C samples showed a charge–discharge plateau close to 3.4 V. The discharge capacities at different C-rates increase initially and then decline at higher calcination temperatures. The NVP@C electrode obtains the best performances in terms of specific discharge capacities and rate capability when the calcining temperature reaches 850 °C. It exhibits an initial specific discharge capacity of 103 mA h g^{-1} at

0.1C rate and still maintains 75 mA h g^{-1} at 5C. The discharge capacities for all samples at different C-rates are compiled in Table S4 (ESI†).

Fig. 4(a) displays the initial charge/discharge curves at various calcination temperatures within the potential range of 2.8–4 V, conducted at a 0.1C rate. As shown in Fig. 4(a), all electrodes showed a charge/discharge plateau close to 3.4 V. The specific discharge capacities of NVP@C demonstrated an increase with higher calcination temperatures ranging from 750 to 900 °C. At a rate of 0.1C, the NVP@C-850 °C (NH3) electrode displayed specific discharge capacities of 103 mA h g^{-1}. Fig. 4(b) illustrates the initial GCD profiles of the NVP@C composites at different calcination temperatures at 1C. All the samples exhibit a charge/discharge plateau at around 3.42–3.50 and 3.34–3.36 V, analogous to a V^{4+}/V^{3+} redox couple during the transformation between $Na_3V_2(PO_4)_3/NaV_2(PO_4)_3$.[26] From these curves, two distinct potential plateaus are observed during the discharge cycles, consistent with the findings obtained from CV curves. As shown in Fig. 4(a) and (b), the voltage plateau of the sample calcined at 850 °C is notably flatter and longer compared to other NVP@C samples, featuring minimum polarization between the charge and discharge plateaus. This behavior suggests improved kinetics of electron transport in the respective sample. The specific discharge capacities at 1C rate are 18, 72, 98, and 90 mA h g^{-1} at temperatures of 750, 800, 850, and 900 °C, respectively. Fig. 4(c) shows the rate performance of different NVP@C electrodes for 4 cycles at different C rates (0.1C–5C). The figure illustrates that the specific discharge capacity decreases as the current density increases. NVP@C calcined at 850 °C possessed enhanced rate capability and lesser capacity decay through all C-rate. At a rate of 0.1C, it demonstrates an initial specific discharge capacity of 103 mA h g^{-1} and retains a discharge capacity of 75 mA h g^{-1} even at 5C, as shown in Fig. 4(c). When the C rate was retained at 0.1C after being increased to 5C, the NVP electrode (750, 800, 850, and 900 °C) recovered a discharge capacity of 33, 78, 103, and 99 mA h g^{-1}, respectively.

Fig. 4(d) displays the discharge capacity and coulombic efficiency *versus* cycle numbers for the different NVP@C electrodes cycled (250 cycles) at 2C. After 250 cycles, the NVP electrodes, NH1, NH2, NH3, and NH4 provided discharge capacities of 14, 45, 85, and 80 mA h g^{-1}, respectively, with 99% capacity retentions for all electrodes. Furthermore, NVP calcined at 850 °C exhibited a coulombic efficiency of approximately 98% in the initial cycle and maintained a coulombic efficiency of nearly 100% after the 250th cycle. Fig. 4(d) demonstrates that the NVP@C (850 °C) electrode delivered a higher specific discharge capacity than the other three electrodes. The excellent electrochemical performance of the NH3 electrode shows that the optimal calcination temperature for the synthesis of NVP is 850 °C.

The stability of NVP at optimum calcination temperature (850 °C) over 2000 cycles is shown in Fig. 5. Fig. 5(a) displays the charge/discharge curves of NVP@C at a high C-rate of 10C. It was observed that the voltage plateaus almost remain constant except for a slight decay in the capacity, representing electrochemical stability under prolonged cycling. The cyclic stability of NVP@C at 10C after 2000 cycles is displayed in Fig. 5(b). The

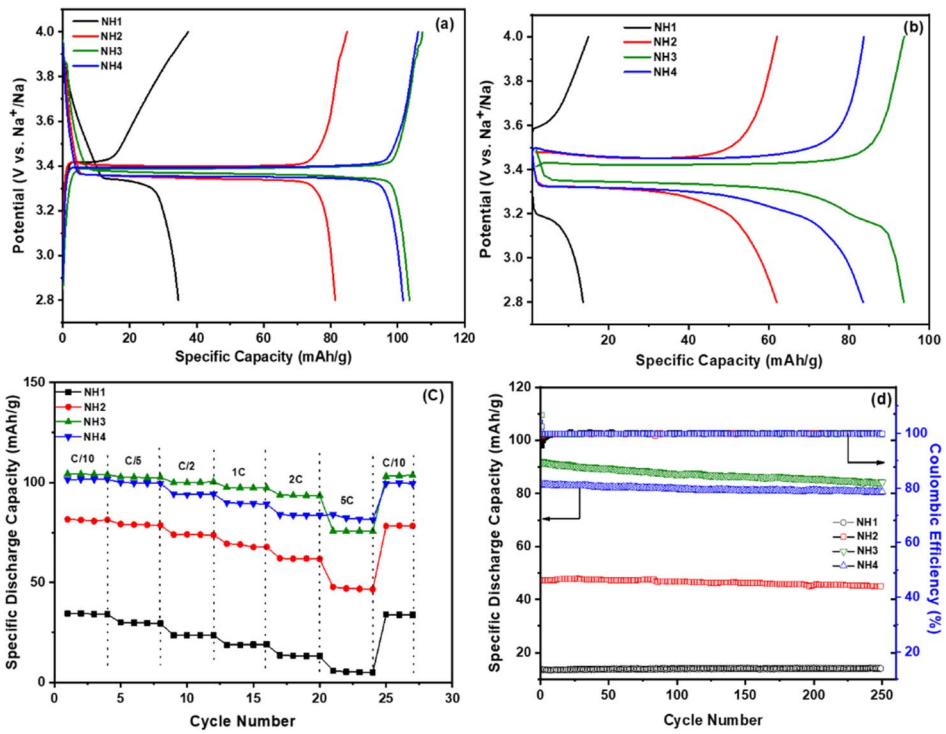

Fig. 4 (a) The first charge–discharge profiles at 0.1C (b) first charge–discharge profiles at 1C, (c) rate capability of NVP@C at different temperatures in a potential range of 2.8–4.0 V *vs.* Na/Na^+, (d) cyclability at a rate of 2C.

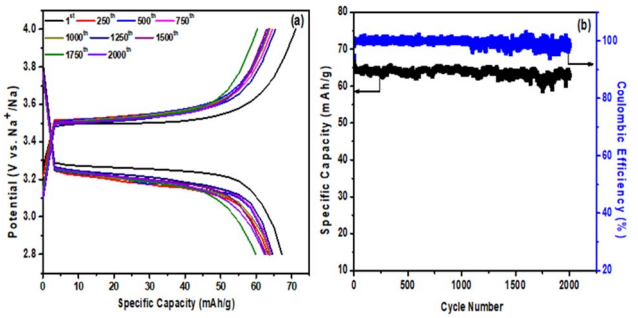

Fig. 5 (a) The galvanostatic charge–discharge profiles at 10C, (b) cyclic performance at 10C of NVP@C calcined at temperature 850 °C.

initial specific discharge capacity reached 67 mA h g^{-1} and was maintained at 63 mA h g^{-1}, with a capacity retention of 94% after 2000 cycles. In addition to the low-capacity fading, the NVP electrode shows coulombic efficiency nearly at 98%, indicating good cycling performance. The cycling performance of the other three electrodes (750 °C, 800 °C, and 900 °C) at 10C is shown in Fig. S8 (ESI†). NVP@C calcined at 750, 800, and 900 °C obtains an initial specific discharge capacity of 2, 27, and 64 mA h g^{-1}, respectively. After 2000 cycles, the capacities are retained at 1, 24, and 50 mA h g^{-1}, respectively. The cycling stability of the NVP@C electrode calcined at 850 °C is higher than that of 750, 800, and 900 °C. Table S5 (ESI†) summarizes the specific discharge capacity at the C rate with the number of cycles and capacity retention of various NVP-based cathodes.

Fig. 6(a) shows the Nyquist plots of NVP@C at various calcination temperatures before charge/discharge. EIS spectra comprise a semicircle at a high and straight slope in a low-frequency region. The sample NH3 has a smaller semicircle diameter, indicating that the charge transfer resistance (R_{ct}) of NVP (502 Ω) is smaller than that of other NVP electrodes (NH1 = 2050 Ω, NH2 = 1343 Ω, NH4 = 842 Ω). Low charge-transfer resistance for NVP@C at 850 °C demonstrates its responsive and rapid electron transportation and hence it has better electrochemical performance, especially the rate performance.

The relationship between Z' and $\omega^{-1/2}$ was depicted (Fig. 6(b)), and the diffusion coefficient of sodium ions was calculated using its slope. The following equation was employed to determine the diffusion coefficient of Na^+:[40]

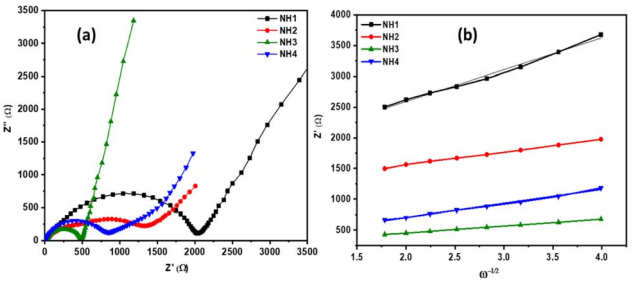

Fig. 6 (a) The Nyquist plots, (b) relationship between real parts of the impedance (Z') and $\omega^{-1/2}$ at low frequencies of the NVP@C calcined at different temperatures.

Table 2 Comparison of electrochemical parameters from Nyquist plot for the NVP@C electrodes

Electrode	R_s (Ω)	R_{ct} (Ω)	σ	D_{Na} (cm^2 s^{-1})
750 °C	22.72	2027	517	3.3×10^{-12}
800 °C	8.47	1334	210	2.0×10^{-11}
850 °C	11.30	490	113	6.9×10^{-11}
900 °C	11	831	228	1.7×10^{-11}

$$D = \frac{R^2T^2}{A^2n^4F^4C^2\sigma^4} \quad (1)$$

$$Z' = R_D + R_L + \sigma\omega^{-1/2} \quad (2)$$

The diffusion coefficients 'D' determined according to eqn (2) are 3.3×10^{-12}, 2.0×10^{-11}, 6.9×10^{-11}, and 1.7×10^{-11} for NH1, NH2, NH3 & NH4 respectively. NVP@C calcined at 850 °C (NH3) exhibits the highest Na^+ diffusion coefficient, indicating that a calcination temperature of 850 °C results in superior microstructure and structural integrity for the material. The improved electrochemical performance is ascribed to the *in situ* carbon coating on NVP@C particles, combined with the suitable microstructure of the electrode material, which facilitates efficient electron/ion transport pathways. The obtained values of R_s, R_{ct}, and D_{Na} are provided in Table 2.

Further, CV and EIS measurements were conducted for a better understanding of the electrode after 2000 cycles at 10C. CVs carried out at a scan rate of 0.1 mV s^{-1} (Fig. 7(a)) showed well-resolved oxidation and reduction peaks except the sample calcined at 750 °C revealing the good reversibility of the electrode at a high current density (10C). Fig. 7(b) represents the results of the EIS analysis conducted after the 2000th cycle. After 2000 cycles, the R_{ct} values of NV@C synthesized at various calcination temperatures are estimated to be ~23 K, ~787, ~373 and, 985 Ω, respectively. The R_{ct} values for samples calcined at 750 and 900 °C exhibit significantly higher values compared to those before cycling. The increase in resistance growth observed in the sample calcined at 800 and 850 °C is the minimum and it is less than before cycling. The phenomenon of a decrease in resistance after cycling was explained by Song *et al.*[41] It may be due to the high surface area and structural defects of the material, which promote irreversible ion insertion

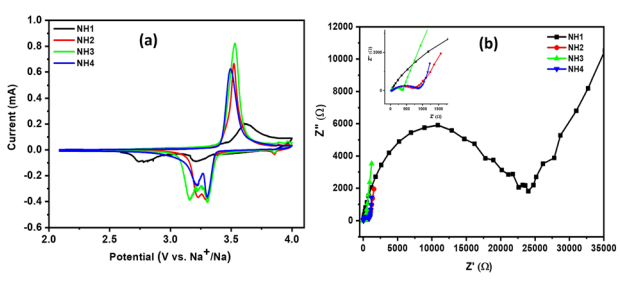

Fig. 7 (a) CV curves, (b) Nyquist plot of NVP electrodes at different calcination temperatures after 2000 cycles at 10C.

into the electrode with cycling, which enhances the electrical conductivity.

4. Conclusions

The NASICON type NVP@C samples have been successfully prepared by hydrothermal method followed by calcination. Analyzing the XRD plots of NVP@C synthesized at varying calcination temperatures, it has been observed that with the increase in temperature, the diffraction peak sharpens, indicating a clear enhancement in crystallinity. The Rietveld refinement confirmed that the NVP@C has a rhombohedral structure with lattice parameters $a = b = 8.71$ Å and $c = 21.83$ Å. The comparison demonstrates that the cell volume of NVP@C increases with the calcination temperature. The optimum NVP@C (850 °C) exhibited a discharge capacity of 103 mA h g^{-1} at 0.1C. The best-performing NVP@C cathode delivers a specific discharge capacity of 67 mA h g^{-1} at a 10C rate and retains 94% of its initial capacity after 2000 cycles. The better electrochemical performance of NVP@C is ascribed to microstructure tuning with optimum carbon coating and improved electronic conductivity achieved through the optimum calcination temperature. The outcome highlights the importance of optimizing the synthetic conditions for preparing efficient cathode materials.

Data availability

The data supporting this article have been included as part of the ESI.†

Author contributions

Ranjit S. Kate – performed experiments, investigation, visualization, original draft preparation, Kaustav Bhattacharjee – analysis of results, writing the paper. Milind V. Kulkarni – supervision & editing. Ramesh J. Deokate – review & editing, supervision. Bharat B. Kale – review & editing, supervision. Ramchandra S. Kalubarme – review & editing, supervision.

Conflicts of interest

There are no conflicts to declare.

Acknowledgements

The authors would like to thank MeitY for its financial support (GG-11/9/2018-EMCD-MeitY) and C-MET Pune for providing research facilities. RSK would like to thank CSIR (File No. 09/1311(11472)/2021-EMR-I) for financial support. RJD would like to thank SERB, TARE fellowship (TAR/22/000037) for research grant support.

References

1 D. Larcher and J. M. Tarascon, Towards greener and more sustainable batteries for electrical energy storage, *Nat. Chem.*, 2015, **7**, 19–29.

2 Q. Ni, Y. Bai, F. Wu and C. Wu, Polyanion-type electrode materials for sodium-ion batteries, *Adv. Sci.*, 2017, **4**, 1600275.

3 H. Pan, Y. S. Hu and L. Chen, Room-temperature stationary sodium-ion batteries for large-scale electric energy storage, *Energy Environ. Sci.*, 2013, **6**, 2338–2360.

4 C. Fang, Y. Huang, W. Zhang, J. Han, Z. Deng, Y. Cao and H. Yang, Routes to High Energy Cathodes of Sodium-Ion Batteries, *Adv. Energy Mater.*, 2016, **6**, 1501727.

5 V. Palomares, M. Casas-Cabanas, E. Castillo-Martínez, M. H. Han and T. Rojo, Update on Na-based battery materials. A growing research path, *Energy Environ. Sci.*, 2013, **6**, 2312–2337.

6 G. Xu, A. Kushima, J. Yuan, H. Dou, W. Xue, X. Zhang, X. Yan and J. Li, Ad hoc solid electrolyte on acidized carbon nanotube paper improves cycle life of lithium-sulfur batteries, *Energy Environ. Sci.*, 2017, **10**, 2544–2551.

7 F. Cheng, J. Liang, Z. Tao and J. Chen, Functional materials for rechargeable batteries, *Adv. Mater.*, 2011, **23**, 1695–1715.

8 B. Dunn, H. Kamath and J. M. Tarascon, Electrical energy storage for the grid: A battery of choices, *Science*, 2011, **334**, 928–935.

9 N. Yabuuchi, M. Kajiyama, J. Iwatate, H. Nishikawa, S. Hitomi, R. Okuyama, R. Usui, Y. Yamada and S. Komaba, P2-type Nax Fe1/2 Mn1/2[O2 made from earth-abundant elements for rechargeable NaÂ batteries, *Nat. Mater.*, 2012, **11**, 512–517.

10 H. Hou, C. E. Banks, M. Jing, Y. Zhang and X. Ji, Carbon Quantum Dots and Their Derivative 3D Porous Carbon Frameworks for Sodium-Ion Batteries with Ultralong Cycle Life, *Adv. Mater.*, 2015, **27**, 7861–7866.

11 J. Kim, R. Ponraj, A. G. Kannan, H. W. Lee, R. Fathi, R. Ruffo, C. M. Mari and D. K. Kim, Diffusion behavior of sodium ions in Na0.44MnO2 in aqueous and non-aqueous electrolytes, *J. Power Sources*, 2013, **244**, 758–763.

12 Y. Wang, R. Xiao, Y. S. Hu, M. Avdeev and L. Chen, P2-Na0.6 [Cr0.6 Ti0.4]O2 cation-disordered electrode for high-rate symmetric rechargeable sodium-ion batteries, *Nat. Commun.*, 2015, **6**, 1–9.

13 Y. You and A. Manthiram, Progress in High-Voltage Cathode Materials for Rechargeable Sodium-Ion Batteries, *Adv. Energy Mater.*, 2018, **8**, 1–11.

14 Z. Jian, Y. S. Hu, X. Ji and W. Chen, NASICON-Structured Materials for Energy Storage, *Adv. Mater.*, 2017, **29**, 1601925.

15 S. Chen, C. Wu, L. Shen, C. Zhu, Y. Huang, K. Xi, J. Maier and Y. Yu, Challenges and Perspectives for NASICON-Type Electrode Materials for Advanced Sodium-Ion Batteries, *Adv. Mater.*, 2017, **29**, 1–21.

16 L. Wang, Y. Lu, J. Liu, M. Xu, J. Cheng, D. Zhang and J. B. Goodenough, A superior low-cost cathode for a Na-Ion battery, *Angew. Chem., Int. Ed.*, 2013, **52**, 1964–1967.

17 D. Wessells, R. A. Huggins and Y. Cui, Copper hexacyanoferrate battery electrodes with long cycle life and high power, *Nat. Commun.*, 2011, **2**, 2–6.

18 C. Guo, K. Zhang, Q. Zhao, L. Pei and J. Chen, High-performance sodium batteries with the 9,10-

anthraquinone/CMK-3 cathode and an ether-based electrolyte, *Chem. Commun.*, 2015, **51**, 10244–10247.
19 M. Pasta, C. D. Wessells, N. Liu, J. Nelson, M. T. McDowell, R. A. Huggins, M. F. Toney and Y. Cui, Full open-framework batteries for stationary energy storage, *Nat. Commun.*, 2014, **5**, 1–9.
20 W. Lee, R. Y. Wang, M. Pasta, S. W. Lee, N. Liu and Y. Cui, Manganese hexacyanomanganate open framework as a high-capacity positive electrode material for sodium-ion batteries, *Nat. Commun.*, 2014, **5**, 1–6.
21 H. Ha, S. H. Woo, D. Mok, N. S. Choi, Y. Park, S. M. Oh, Y. Kim, J. Kim, J. Lee, L. F. Nazar and K. T. Lee, Na4-αM2+α/2(P2O 7)2 (2/3 ≤ α ≤ 7/8, M = Fe, Fe 0.5Mn0.5, Mn): A promising sodium ion cathode for na-ion batteries, *Adv. Energy Mater.*, 2013, **3**, 770–776.
22 R. S. Kate, H. Jadhav, U. V Kawade, K. Bhattacharjee, M. Kulkarni, R. J. Deokate, B. B Kale and R. S. Kalubarme, Critical Review of recent progress and challenges of polyanion Na3V2 (PO4) 3 cathode material in rechargeable sodium-ion batteries, *J. Mater. Chem. A*, 2024, **12**, 7418–7451.
23 Z. Jian, W. Han, X. Lu, H. Yang, Y. S. Hu, J. Zhou, Z. Zhou, J. Li, W. Chen, D. Chen and L. Chen, Superior electrochemical performance and storage mechanism of Na3V2(PO4)3 cathode for room-temperature sodium-ion batteries, *Adv. Energy Mater.*, 2013, **3**, 156–160.
24 Y. Lim, H. Kim, R. A. Shakoor, Y. Jung and J. W. Choi, Electrochemical and Thermal Properties of NASICON Structured Na3V2(PO4)3 as a Sodium Rechargeable Battery Cathode: A Combined Experimental and Theoretical Study, *J. Electrochem. Soc.*, 2012, **159**, A1393–A1397.
25 W. Song, X. Ji, Z. Wu, Y. Zhu, Y. Yang, J. Chen, M. Jing, F. Li and C. E. Banks, First exploration of Na-ion migration pathways in the NASICON structure Na3V2(PO4)3, *J. Mater. Chem. A*, 2014, **2**, 5358–5362.
26 H. Li, X. Bi, Y. Bai, Y. Yuan, R. Shahbazian-yassar, C. Wu, F. Wu, J. Lu and K. Amine, High-Rate, Durable Sodium-Ion Battery Cathode Enabled by Carbon-Coated Micro-Sized Na3V2(PO4)3 Particles with Interconnected Vertical Nanowalls, *Adv. Mater. Interfaces*, 2016, **2**, 1–8.
27 E. Wang, W. Xiang, R. Rajagopalan, Z. Wu, J. Yang, M. Chen, B. Zhong, S. X. Dou, S. Chou, X. Guo and Y. M. Kang, Construction of 3D pomegranate-like Na3V2(PO4)3/conducting carbon composites for high-power sodium-ion batteries, *J. Mater. Chem. A*, 2017, **5**, 9833–9841.
28 R. S. Kate, S. V. Kadam, M. V. Kulkarni, R. J. Deokate, B. B. Kale and R. S. Kalubarme, Highly stable and nanoporous Na3V2 (PO4) 3@ C cathode material for sodium-ion batteries using thermal management, *J. Energy Storage*, 2023, **74**(202), 109245.
29 Y. Fang, L. Xiao, X. Ai, Y. Cao and H. Yang, Hierarchical Carbon Framework Wrapped Na3V2(PO4)3 as a Superior High-Rate and Extended Lifespan Cathode for Sodium-Ion Batteries, *Adv. Mater.*, 2015, **27**, 5895–5900.
30 W. Duan, Z. Zhu, H. Li, Z. Hu, K. Zhang, F. Cheng and J. Chen, Na3V2(PO4)3@C core–shell nanocomposites for rechargeable sodium-ion batteries, *J. Mater. Chem. A*, 2014, **2**, 8668–8675.
31 H. Li, L. Shen, K. Yin, J. Ji, J. Wang, X. Wang and X. Zhang, Facile synthesis of N-doped carbon-coated Li4Ti5O12 microspheres using polydopamine as a carbon source for high rate lithium ion batteries, *J. Mater. Chem. A*, 2013, **1**, 7270–7276.
32 L. Lutterotti and P. Scardi, Simultaneous structure and size-strain refinement by the Rietveld method, *J. Appl. Crystallogr.*, 1990, **23**, 246–252.
33 I. V. Zatovsky, NASICON-type Na3V2(PO4)3, *Acta Crystallogr., Sect. E: Struct. Rep. Online*, 2010, **66**, I12-U194.
34 K. Bhattacharjee, S. P. Pati, G. C. Das, D. Das and K. K. Chattopadhyay, Effect of particle size distribution on the structure, hyperfine, and magnetic properties of Ni0.5Zn0.5Fe2O4 nanopowders, *J. Appl. Phys.*, 2014, **116**, 233907.
35 H. Toby, R factors in Rietveld analysis: How good is good enough?, *Powder Diffr.*, 2006, **21**, 67–70.
36 R. Zhang, Y. Zhang, K. Zhu, F. Du, Q. Fu, X. Yang, Y. Wang, X. Bie, G. Chen and Y. Wei, Carbon and RuO2 binary surface coating for the Li 3V2(PO4)3 cathode material for lithium-ion batteries, *ACS Appl. Mater. Interfaces*, 2014, **5**, 12523–12530.
37 W. Li, Z. Yao, C. ao Zhou, X. Wang, X. Xia, C. Gu and J. Tu, Boosting High-Rate Sodium Storage Performance of N-Doped Carbon-Encapsulated Na3V2(PO4)3 Nanoparticles Anchoring on Carbon Cloth, *Small*, 2019, **15**, 1–10.
38 W. Shen, H. Li, C. Wang, Z. Li, Q. Xu, H. Liu and Y. Wang, Improved electrochemical performance of the Na3V2(PO4)3 cathode by B-doping of the carbon coating layer for sodium-ion batteries, *J. Mater. Chem. A*, 2015, **3**, 15190–15201.
39 F. Li, Y. E. Zhu, J. Sheng, L. Yang, Y. Zhang and Z. Zhou, GO-induced preparation of flake-shaped Na3V2(PO4)3@rGO as high-rate and long-life cathodes for sodium-ion batteries, *J. Mater. Chem. A*, 2017, **5**, 25276–25281.
40 X. Jiang, F. Hu, W. Wang, J. Qiu and X. Zheng, Hierarchical polyhedron K2CoFe(CN)6 as promising cathode for rechargeable batteries, *J. Alloys Compd.*, 2019, **774**, 315–320.
41 R. Song, H. Song, J. Zhou, X. Chen, B. Wu and H. Y. Yang, Hierarchical porous carbon nanosheets and their favorable high-rate performance in lithium ion batteries, *J. Mater. Chem.*, 2012, **22**, 12369–12374.